

Learning to Downsample for Segmentation of Ultra-High Resolution Images

Chen Jin¹, Ryutaro Tanno^{1,2}
Thomy Mertzanidou¹, Eleftheria Panagiotaki¹, Daniel C. Alexander¹

¹ Centre for Medical Image Computing, University College London, UK

² Healthcare Intelligence, Microsoft Research Cambridge, UK
chen.jin@ucl.ac.uk, rytanno@microsoft.com

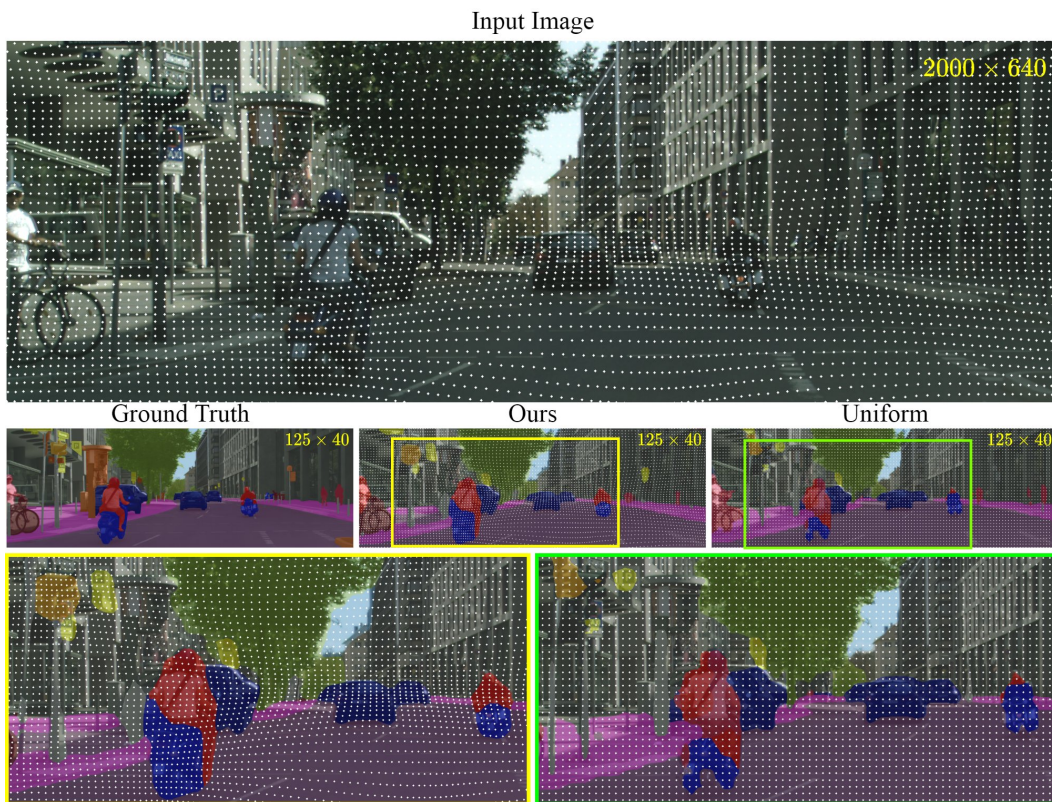


Figure 1: Semantic Segmentation with Deformed Downsampling. We propose a method for learning to downsample ultra high-resolution images (top-row) that reflects the importance of each location. The aim is to preserve information that guides segmentation and ignore image content that does not contribute thereby enabling low-cost semantic segmentation on low-resolution downsampled images. This strategy helps identify small regions such as the people in the figure; see masked ground truth and predictions in middle-row. We introduce the *deformation module*, a learnable "downsampler", that can be jointly trained with the *segmentation module*, to adapt sampling density according to importance at each location (white dots on the images). The *deformation module* is lightweight and can be flexibly integrated into existing semantic segmentation architectures. Compared to baseline standard uniform downsampling (referred to as "Uniform") our method (referred to as "Ours") samples more densely at important semantic regions and leads to more accurate segmentation (see bottom-row).

Abstract

Segmentation of ultra-high resolution images with deep learning is challenging because of their enormous size, often millions or even billions of pixels. Typical

solutions drastically downsample the image uniformly to meet memory constraints, implicitly *assuming all pixels equally important* by sampling at the same density at all spatial locations. However this assumption is not true and compromises the performance of deep learning techniques that have proved powerful on standard-sized images. For example with uniform downsampling, see green boxed region in Fig. 1, the rider and bike do not have enough corresponding samples while the trees and buildings are oversampled, and lead to a negative effect on the segmentation prediction from the low-resolution downsampled image. In this work we show that learning the spatially varying downsampling strategy jointly with segmentation offers advantages in segmenting large images with limited computational budget. Fig. 1 shows that our method adapts the sampling density over different locations so that more samples are collected from the small important regions and less from the others, which in turn leads to better segmentation accuracy. We show on two public and one local high-resolution datasets that our method consistently learns sampling locations preserving more information and boosting segmentation accuracy over baseline methods.

1 Introduction

Many automated processes such as auto-piloting, geospatial analysis and medical image processing rely on good semantic segmentation over ultra-high resolution images with millions or even billions of pixels. Exemplary applications include urban scene analysis with camera array images ($> 25000 \times 14000$ pixels)[1], geospatial analysis with satellite images ($> 5000 \times 5000$ pixels) [2] and histopathological analysis with whole slide images ($> 10,000 \times 10,000$ pixels) [3]. Challenges arise when applying deep learning (DL) methods on those ultra-high resolution, like those in [3, 4, 5], due to GPU memory constraints.

To speed up performance and adapt to memory requirements or data transmission latency, it is common to uniformly downsample the whole input images, then train the segmentation network and make predictions at lower resolution (locally or remotely), and finally upsample back to the original resolution (as summarised in Fig. 3 (a)). However, the uniform downsampling approach, which we refer to as “uniform”, treats all pixels as equally important. This generally leads to reduced performance when directly applying DL approaches, which perform best on data sets where images have more manageable size like [6, 7, 8]. For example, in segmentation problems that require finding “needles in a haystack” where a certain small positive foreground is more important than the rest large negative background (e.g., like tumors in histology images as in Fig. 2 (a)), more samples should be drawn from foreground than background and uniform downsampling may be suboptimal.

Based on a similar intuition, Marin *et al.*[5] recently postulated that denser sampling around object boundaries is important to the segmentation task and thus proposed a method that improves upon uniform downsampling by sampling pixels non-uniformly based on the prediction of a separate boundary-detection model, as summarised in Fig. 3 (b). However such approach would lead to sub-optimal segmentation performance in datasets where annotated regions of interest are not necessarily based on object edges, but higher level context and semantic information as illustrated in Fig. 2 (a). For example, the annotated cancer regions in Fig. 2 (b) contain tissue and nuclei, and the annotated Forest and Agriculture regions in Fig. 2 (c) contain different types of plants, and all those unannotated objects may confuse the edge-detection driven “optimal edge” downsampling network and reduce segmentation accuracy.

In this work, we introduce *deformation module*, a learnable downsampler, that is jointly trained with any *segmentation model* to adapt sampling density according to the local image contents. The downsampled image guided by the *deformation module* results in a deformed low-resolution image and hence the name. Specifically, the *deformation module* processes a downsampled version of the given large volume high-resolution image and estimates a sampling density distribution to downsample a low-resolution image while preserving information differently over different locations. The *deformation module* can be trained jointly in an end-to-end fashion with the segmentation network to optimise the pixel-wise segmentation performance thus optimise sampling flexibly. Additionally, the *deformation module* is a light-weight learnable downsampler, and can be used to augment a wide range of existing segmentation architectures (as we show empirically). We demonstrate the general utility of our approach using two public and one local datasets from different domains. DeepGlobe[10] and a local Prostate Cancer Histology dataset (“PCa-Histo”) are datasets consisting of ultra high-resolution aerial and whole-slide-images.

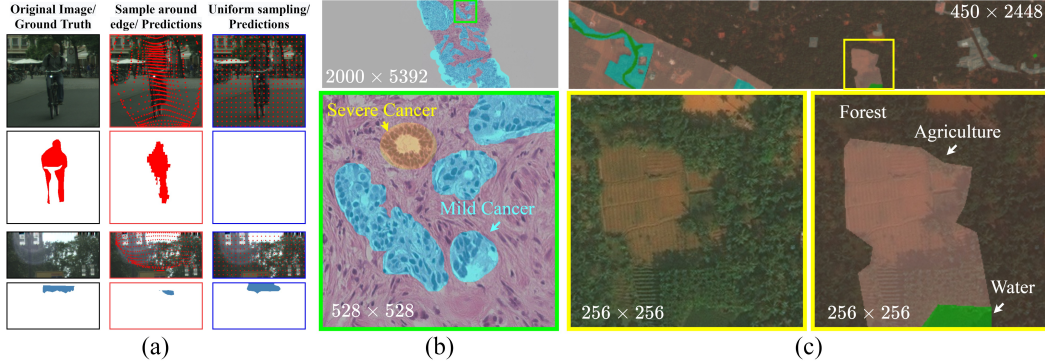


Figure 2: Examples and challenges of downsampling ultra-high resolution images: (a) Binary segmentation examples from Cityscapes dataset [9] showing the "optimal edge" [5] method, with fixed sampling density around object edges, performing differently at different locations, and therefore won't guarantee overall optimal result. We verify such weakness of the "optimal edge" [5] method with strict elementary controlled motivational study whose full details are provided in Appendix. (b) Prostate cancer annotated on a histological image and (c) a remote sensing image from DeepGlobe dataset [10]. Both (b) and (c) show that adaptive downsampling methods are required to sample differently at each location, but simple object edge-guided methods will not work when annotated regions are based on higher level knowledge.

We also use the popular Cityscapes dataset [9] since it provides a familiar platform for demonstration and evaluation. In all datasets we show that a light-weight implementation of the *deformation module* can consistently boost the segmentation performance with little extra computational cost.

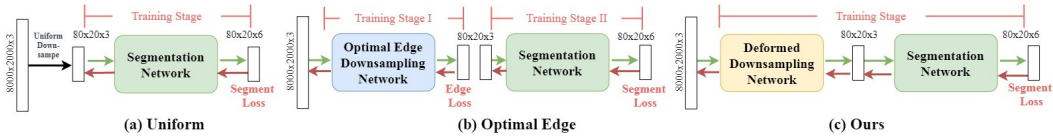


Figure 3: Comparing training pipelines of (a) "uniform" (b) "optimal edge" and (c) Our proposed "Deformation" approaches. Low resolution predictions are uniform/non-uniform upsampled to original resolution at inference.

2 Related Works

Different sampling strategies have been developed to improve performance of CNNs. We group these methods into three main categories: feature aggregating and sampling, sampling as pre-processing for image classification, sampling as pre-processing for image segmentation.

2.1 Feature aggregating and sampling

A key problem in segmentation community is the importance of using multiple scale features. Various multi-scale architectures [11, 6, 12] have been developed to aggregate features either from different layers or from multiple inputs with different resolutions and were proved to achieve good segmentation accuracy. Such an aggregation process can be achieved either in sequential manner such as in RefineNet [13], in parallel like in U-net [14] via skip connections and its variants [15, 16], or with a combination of the two like the high-resolution network (HRNet) [7]. While multi-scale architectures have shown the importance of multiple scale features, the aggregation process is less efficient because input images need to be re-scaled multiple times to obtain multiple scale features. With similar appreciation to importance of features at multiple scales, Deformable convolutional networks (DCNs) [17] propose to learn sampling offsets, conditioned on the input from previous layers, to dynamically adjust sampling receptive field in the standard convolution. DCNs showed that a carefully learnt feature sampling in the last few layers of the network can improve segmentation performance. Although DCNs share similarities with our approach, they are complementary to ours because we focus on learning a better downsampling strategy prior to segmentation, so that maximal information can be kept at minimal computation cost at segmentation.

2.2 Sampling as pre-processing for image classification

With intuition that per-image labelling can be predicted by improved sampling of the image or even a sub-region to reduce computation cost, several learnt image-sampling methods have been developed. Spatial Transformer Networks (STN) [18] introduce a layer that estimates a parametrized affine, projective and splines transformation from an input image to recover data distortions and thereby improve image classification accuracy. Similarly, [19] learn a saliency-based layer and "zoom-in" to salient regions when sampling an input image. Similar approaches have been developed to reduce computational burden on processing ultra-high resolution images. In [20] attention weights are learned over the input image to sample a small informative subset for the downstream per-image classification task. A related approach was introduced in [21] based on the use of saliency maps for the task of breast cancer screening with high-resolution mammography images. However, the optimisation goal of learning a spatially downsampling strategy for per-image classification is different to the per-pixel segmentation task. The difference is that for a per-image task the primary optimisation goal is to identify one or few regions that best represent per-image label to sample denser. But for a per-pixel task it is also important to learn to balance how much denser to sample at each location. In a segmentation task, denser sampling at one location may compromise segmentation accuracy at nearby locations, as we will show in this work, and therefore more careful regularisation is needed.

2.3 Sampling as pre-processing for image segmentation

With respect to the importance of multiscale features while reducing the cost of segmenting a large image, region-proposal approaches, originated in object detection tasks, split the segmentation task into two by first detecting the object and sampling the optimal crop and then segmenting the object from either the cropped image [22, 23] or features [24, 25]. While typical region proposal approaches have shown that learning to detect region crop around a target object can ease the segmentation that follows, [26] propose to jointly train a crop-sampling network that exemplifies the trade-off configuration between crop size and downsampling rate for each crop at each location. This maximizes the downstream segmentation performance of ultra-high resolution images. However these approaches have high computational cost for optimal segmentation performance, because each cropped region needs to be segmented individually. Non-uniform grid representation is becoming a common approach in computer vision to alleviate the memory cost by modifying input images in a non-uniform fashion to improve efficiency, such as meshes [27, 28], signed distance functions [29], and octrees [30]. However none of those approaches is optimised specifically for segmentation. The work most similar to ours is "optimal edge" [5], which reduces the computational cost prior to segmentation by separately training a downsampling network which encourages denser sampling close to object edges and thus can improve segmentation accuracy from low-resolution images. Here in this work we argue that a jointly trained downsampling network based on segmentation performance at each location is better-suited for this task and can provide improved performance.

3 Methods

In this section, we first formulate the basic components associated with this study in section 3.1. We then propose the *deformation module* in section 3.2, a learnable downsampler jointly trained with the *segmentation module*, that learns spatially varying non-uniform downsampling over different locations.

3.1 Problem Formulation

Sampling method: Let $\mathbf{I} \in \mathbb{R}^{H \times W \times C}$ be a high-resolution image of an arbitrary size H, W, C , which denote the height, width and channels respectively. Next, a sampler \mathbf{G} takes \mathbf{I} as input and computes a downsampled image $\mathbf{J} = \mathbf{G}(\mathbf{I})$, where $\mathbf{J} \in \mathbb{R}^{h \times w \times C}$. Following the definition of grid sampler introduced in [18], consider a relative coordinate system such that $\mathbf{I}[\mathbf{u}, \mathbf{v}]$ is the pixel value of original image \mathbf{I} where $\mathbf{u}, \mathbf{v} \in [0, 1]$. And an absolute coordinate system such that $\mathbf{J}[i, j]$ is the pixel value of the downsampled image \mathbf{J} at coordinates (i, j) for $i \in \{1, 2, \dots, h\}, j \in \{1, 2, \dots, w\}$. Essentially, the sampler \mathbf{G} computes a mapping between (i, j) and (\mathbf{u}, \mathbf{v}) . Practically, sampler \mathbf{G} contains two functions $\{\mathbf{g}^0, \mathbf{g}^1\}$, such that $\mathbf{u}[i, j] = \mathbf{g}^0(i, j), \mathbf{v}[i, j] = \mathbf{g}^1(i, j)$. So for a downsampled image $\mathbf{J} = \{\mathbf{J}[i, j]\}$, we have sampling operator:

$$\mathbf{J}[i, j] := \mathbf{I}[\mathbf{g}^0(i, j), \mathbf{g}^1(i, j)] \quad (1)$$

Given the above notation, the "uniform" approach will have sampler $\mathbf{G}_{\mathbf{u}}$ with sampling functions $\{\mathbf{g}_{\mathbf{u}}^0, \mathbf{g}_{\mathbf{u}}^1\}$, such that $\mathbf{g}_{\mathbf{u}}^0(i, j) = (i-1)/(h-1), \mathbf{g}_{\mathbf{u}}^1(i, j) = (j-1)/(w-1)$.

Segmentation and non-uniform upsampling: In this work we discuss model agnostic downsampling and upsampling methods, and therefore any available Segmentation model can be applied. Here we denote the segmentation network \mathbf{S}_ϕ , parameterised by ϕ , that takes as an input a downsampled image \mathbf{J} and makes a prediction $\mathbf{S}_\phi(\mathbf{J})$ in the low resolution space. Specifically, our results are based on HRnet-w48[7] and PSP-net[15]. As in prior work[5], upsampling consists of the reverse of downsampling and interpolation. The reverse of downsampling is achieved with a reverse sampler $\mathbf{G}^{-1}()$, which reverses the mapping of each pixel at coordinates (i, j) of the sampled image \mathbf{J} back to coordinates (u, v) in the original high-resolution image domain. Then an interpolator $\mathbf{Int}()$ is applied to calculate the missing pixels to get $\mathbf{Int}(\mathbf{G}^{-1}(\mathbf{J}))$. In this work we use nearest neighbour (implementation available in Scipy[31]).

Evaluation matrix: Typically, evaluation with intersection over union (IoU) is only performed at the end of inference, i.e. after upsampling, between the upsampled prediction and the label. However, such evaluation only reflects the compound error of sampling and segmentation. As in this work we are interested in the quality of sampling, we therefore apply the same downsampling and non-uniform upsampling process to the original label \mathbf{Y} , to get a recovered label $\mathbf{Y}' = \mathbf{Int}(\mathbf{G}^{-1}(\mathbf{G}(\mathbf{Y})))$. To this end, IoU could be calculated between the recovered label \mathbf{Y}' and the original label \mathbf{Y} , which we refer to as IoU(label recover). The IoU(label recover) can be treated as a direct evaluation of the error associated both in the downsampling and upsampling process.

3.2 Deformation module: learn non-uniform downsampling for efficient segmentation

We introduce the *deformation module*, a data driven sampling method which learns spatially varying non-uniform downsampling at each spatial location according to its importance to the downstream segmentation task. Fig.4 provides a schematic of the proposed method. The *deformation module* takes a low-resolution version of a high-resolution input image and estimates the deformed sampler (a non-uniform downsampler) that adapts the sampling density at different pixel locations. Then, the *segmentation network* processes the input downsampled image based on the output of *deformation module*, and estimates the corresponding segmentation probabilities. The *deformation module* can be a light weighted CNN architecture with random initialisation like [32], and the segmentation network can be any existing architecture (we will later use two recent and different architectures, namely PSP-net[15] and HRNet [7]).

For each high-resolution image $\mathbf{I} \in \mathbb{R}^{H \times W \times C}$, we compute its lower resolution version $\mathbf{I}_r \in \mathbb{R}^{h_a \times w_a \times C}$. The *deformation module*, D_θ , parametrised by θ , takes the low-resolution image \mathbf{I}_r as input and generates a deformation map $\mathbf{d} = D_\theta(\mathbf{I}_r)$, where $\mathbf{d} \in \mathbb{R}^{h_a \times w_a \times 1}$, that predicts the sampling density at each pixel location. Next, the deformed sampler \mathbf{G}_d is constructed by taking both \mathbf{I} and \mathbf{d} as input and computes the downsampled image $\mathbf{J} = \mathbf{G}_d(\mathbf{I}, \mathbf{d})$, where $\mathbf{J} \in \mathbb{R}^{h \times w \times C}$. Following the same downsampled segmentation pipeline defined earlier, the Deformed Sampled image \mathbf{J} can be fed into the segmentation network, $\mathbf{S}_\phi(\mathbf{J})$, parametrised by ϕ to estimate the corresponding segmentation probabilities. We note here at training the same sampler is applied both to get the downsampled label $\mathbf{G}_d(\mathbf{Y}, \mathbf{d})$ and to calculate the segmentation loss.

Following earlier definitions in Equation 1, the deformed sampler \mathbf{G}_d essentially computes a mapping between (i, j) from sampled image \mathbf{J} and (u, v) from original image \mathbf{I} , such that $\mathbf{u}[i, j] = \mathbf{g}^0(i, j)$, $\mathbf{v}[i, j] = \mathbf{g}^1(i, j)$. As mentioned, we would like to train the deformed sampler \mathbf{G}_d who samples \mathbf{I} denser at high-importance regions as high-intensity regions indicated in the deformation map \mathbf{d} . Inspired by [19] we consider the value at each pixel (i', j') in the deformation map \mathbf{d} as an attractive force $\mathbf{d}(i', j')$ that is pulling surrounding pixels. The force acts on an expanded region defined by a distance kernel¹ $k((i, j), (i', j'))$ so that:

$$\mathbf{g}^0(i, j) = \frac{\sum_{i', j'} \mathbf{d}(i', j') k((i, j), (i', j')) i'}{\sum_{i', j'} \mathbf{d}(i', j') k((i, j), (i', j'))}, \quad \mathbf{g}^1(i, j) = \frac{\sum_{i', j'} \mathbf{d}(i', j') k((i, j), (i', j')) j'}{\sum_{i', j'} \mathbf{d}(i', j') k((i, j), (i', j'))} \quad (2)$$

This formulation holds certain desirable properties that fit our goal: 1) the learnable *deformation module* produces a deformation map with varying sampling density at different regions, the need for this was

¹Practically the distance kernel is a fixed Gaussian convolution with given radius. This radius decided the distance the attraction force can act on, while the degree of force is learnt though deformation map. Follow the empirical recommendation given by [19], we set this radius of at least one forth of the short axis of deformation map.

illustrated in the motivational examples shown earlier; 2) the *deformation module* can naturally fit CNN architecture and preserve differentiability for it to be jointly trained with downstream segmentation loss. This way the sampling density at each location is optimised by segmentation performance rather than a manually designed objective function (e.g. distance to edge as in "optimal edge" [5]).

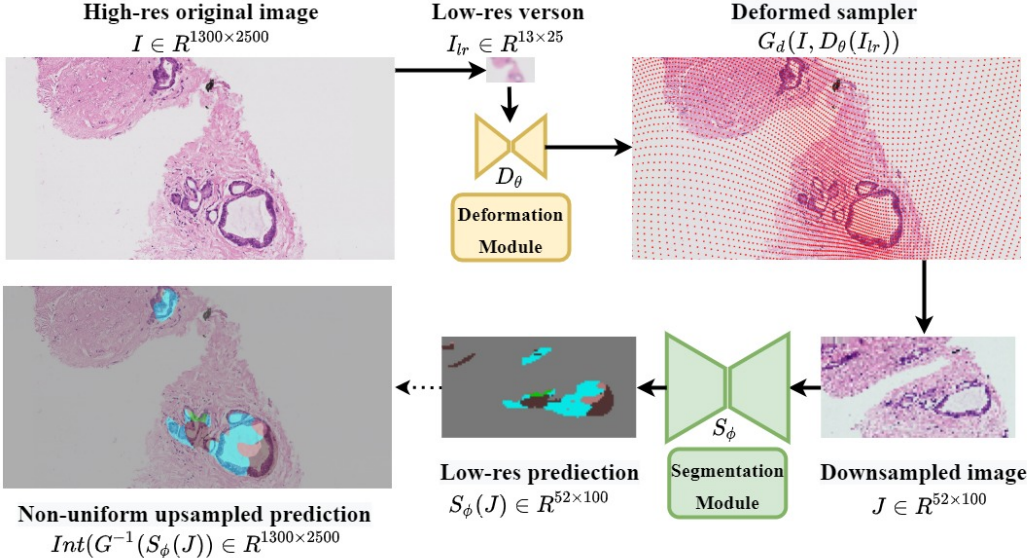


Figure 4: **Architecture schematic.** The deformation module produces the deformation map $\mathbf{d} = D_\theta(\mathbf{I}_{lr})$ that predicts sampling importance weights at different pixel locations. The deformed sampler \mathbf{G}_d samples with different density at each location of the input image \mathbf{I} according to the deformation map, where sampling locations are shown as red dots masked on the original image. The low-resolution downsampled image $\mathbf{J} = \mathbf{G}_d(\mathbf{I}, \mathbf{d})$ is then fed into the segmentation module which makes a prediction $\mathbf{S}_\phi(\mathbf{J})$ in the low-resolution space. At inference time, the prediction is non-uniformly upsampled to the original space in a deterministic manner.

Our method is similar to [19], which however is only explored for image classification tasks. Although transferring the method proposed in [19] to segmentation is straightforward, as discussed in section 2, optimising the joint system at pixel level is not trivial, which we have verified in the Appendix. To discourage the network learning to naively sample denser at easy to segment regions like background, we add a regularisation term in addition to the segmentation loss term. Inspired by the "optimal edge" method [5] we use edge-loss as the regularisation term. Specifically, at training time we generate a target deformation map with fixed sampling density around label-edges and calculate its similarity to the predicted deformation map. To this end, we jointly optimise the parameters $\{\theta, \phi\}$ of both the *deformation module* and the *segmentation module* to minimise the segmentation specific loss function, $\mathcal{L}(\mathbf{J}; \theta, \phi)$ (e.g., focal loss + L2-weight-decay), and the Edge loss, $\mathcal{L}(\mathbf{I}_{lr}; \theta)$ (e.g., MSE loss + L2-weight-decay). We also add a weight term to make sure both losses have comparable magnitudes.

4 Experiments and Results

In this section we evaluate the performance of our deformed downsampling approach on three datasets from different domains as summarised in Table 1, against baselines described in 4.1. {We evaluate the segmentation performance with **IoU** and verify the quality of *deformation module* with **IoU** (label recover). We show that our *deformation module* can learn the spatial variation of optimal non-uniform downsampling, leading to both better segmentation performance and label recovery (Section 4.2). We employ the same training scheme unless otherwise stated. The *deformation module* is defined as a small CNN architecture comprised of 3 convolution layers and ended with a final 1×1 convolutional layer to reduce the dimensionality and a softmax layer for normalisation. The segmentation network was defined as a deep CNN architecture, with HRNetV2-W48[7] used in all datasets, and PSP-net[15] as a sanity check in Cityscapes dataset. We use focal loss as segmentation loss and MSE loss for the edge loss. Full details are provided in Appendix.

Table 1: Dataset summary. More details in Appendix

Dataset	Content	Resolution (pixels)	Number of Classes
Cityscape [9]	Urban scenes	2048 × 1024	19
DeepGlobe [10]	Aerial scenes	2448 × 2448	6
PCa-Histo	Histopathological	1968 ± 216 × 9392 ± 4794	6

4.1 Baselines

We compare our method against two baselines: 1) A uniform downsampling of the input to train the segmentation network followed by uniformly upsampling the prediction ("uniform"); 2) Instead of re-implementing "optimal edge" [5], we simulate a set "optimal edge" directly from labels within our framework, at both training and inference. We generate a set of "optimal edge" downsamplers, each with a fixed sampling density around edges and train a set of segmentation networks. At inference we use the same method to directly generate a set of "optimal edge" downsamplers to downsample and validate the trained segmentation networks. The best performing result is selected and referred to as "optimal edge" result as the second baseline. We note our "optimal edge" result can be seen as an "upper-bound" of [5] because we assume access to the segmentation labels at inference and use them directly to simulate the edge-based sampler, while the original work by [5] train a separate neural network to perform edge detection, whose the output is used by the edge-based downsampler.

4.2 Quantitative and qualitative performance analysis

We plot the following three quantitative results to justify our method: 1) Fig. 17 compare average segmentation performance over all classes on three datasets; 2) Fig. 6 further investigate our method at per-class level, aiming to understand the impact of different object sizes; 3) lastly, in Fig. 7, we exam the impact of downsampled size and ask could our method learn a downsampling strategy enable better trade-off between performance and computation cost. We also provide visual evidence in Fig. 8 and Fig. 9 for further verification and evaluation.

First, our method provide consistent boost in the segmentation performance measured in **mIoU** over both baselines and across all datasets by from from 3% to 10% in absolute **mIoU** over "uniform" (see Fig. 17 and 7).

Such performance boost is also reflected in class-wise performance, as in Fig. 6, our method performs better that both baseline methods for the majority of the low-frequency classes. In high-frequency classes it perfomed better than "optimal edge" and maintained similar performance to the "uniform" approach.

Our mehtod also shown clear advantage on identifying and distinguishing the most clinically important classes, Grade 3 and 4 as in Fig. 6 (c), by boosting accuracy from 15% to 20%. The separation between this two classes is which often referred to as the threshold from healthy to cancer.

It also shown our method can learn a downsampling strategy better preserve information and enable a better trade-off. See red line in Fig. 7 indicated to achieve same final prediction accuracy, the "uniform" baseline require to calculate 50% more pixels on Cityscapes dataset, while on DeepGlobe even at a size 10 times larger than ours, as indicated by red line, "uniform" fail to outperform the ours. Putting quantitative evidence together, we shown our method can efficiently learn where to "invest" the limited budget of pixels at downsampling to achieve highest overall return in segmentation accuracy.

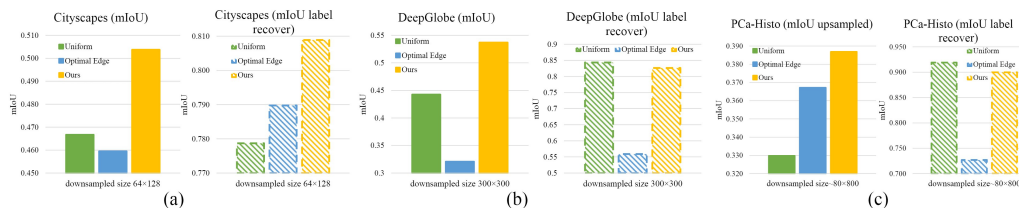


Figure 5: Quantitative comparison of segmentation performance with our learn to downsample strategy versus two baseline downsampling methods, in terms of **mIoU** and **mIoU** label recover. Results are from three datasets: (a) Cityscapes[9] (b) DeepGlobe[10] and a local prostate cancer histology dataset (PCa-Histo).

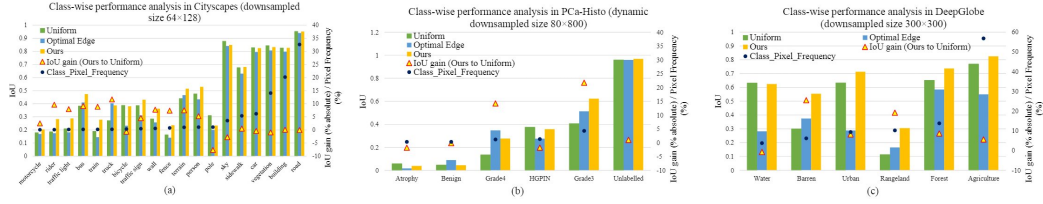


Figure 6: Class-wise IoU analysis on (a) Cityscapes[9] at downsampled sizes of 64×128 ; (b) PCaHisto at dynamic downsampled size of 80×800 ; (c) DeepGlobe[10] at downsampled sizes of 300×300 . Despite absolute **IoU**, relative **mIoU** gain with our method over "uniform" baseline is shown. Classes are ordered with increasing pixel frequency which also indicated in each plot.

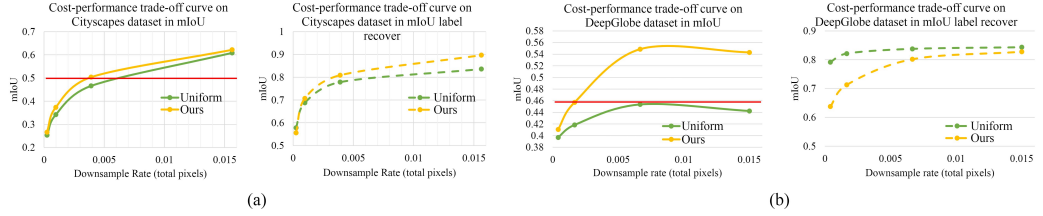


Figure 7: Cost-performance trade-offs in terms of **mIoU** and **mIoU** label recovery on (a) Cityscapes dataset [9] and (b) DeepGlobe dataset [10]. Downsample rate is calculated by divide the total number of pixels after downsampling by original, which determines the size of the input and reflects the amount of computation required.

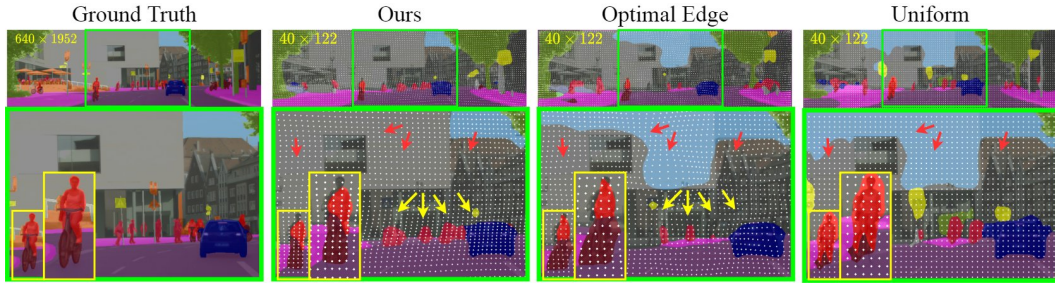


Figure 8: Examples on Cityscapes [9] where segmentation are performed on 16 times (at each dimension) downsampled images. Predictions are masked over and sampling locations are shown in white dots.

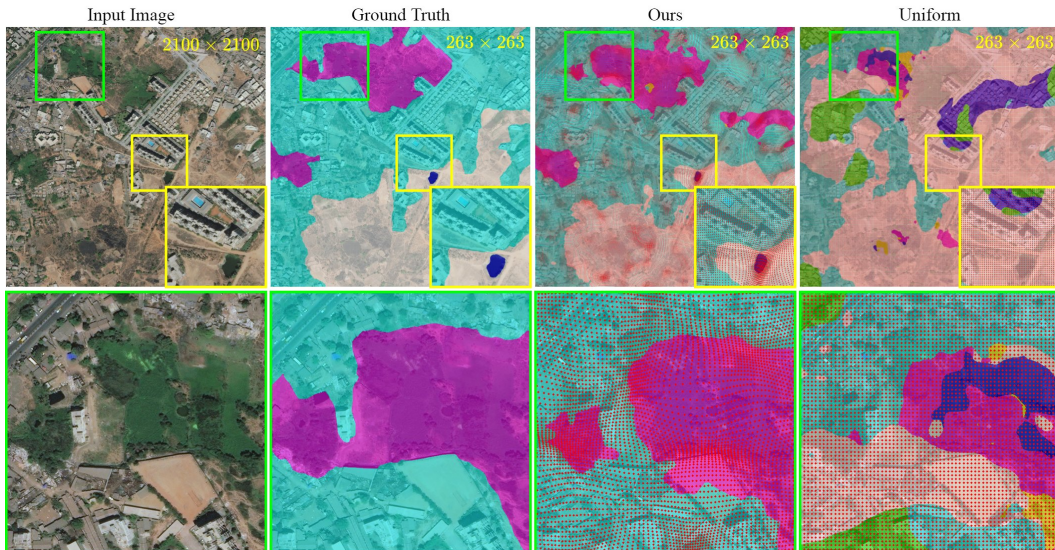


Figure 9: Qualitative example on DeepGlobe dataset [10] where segmentation performed on 8 times (at each dimension) downsampled image. Predictions are masked over and sampling locations are shown in red dots.

4.3 Evaluation and understanding

Visual results from Fig. 8 and Fig. 9 shown our method clearly picked the advantage of the "optimal edge" approach by sampling denser at small objects (e.g. rider and bike in Fig. 8 and water in blue annotation in the yellow boxed region in Fig. 9). While our method further improved sampling by learning a better generalisation on larger objects (e.g. sky (blue) as in Fig. 8 and forest (purple)) in Fig. 9.

On examining the quality of the learnt downsampler with **mIoU** label recover, the results on cityscapes dataset (Fig. 17 (a)) verified our learnt downsampler can better keep information and enable better label recovering. While the **mIoU** label recover with our method on DeepGlobe (Fig. 17 (b)) and PCa-Histo (Fig. 17 (c)) did not perform better but close to "uniform" baseline, the significant improvement over the "optimal edge" baseline demonstrated the deformation module is efficiently learning. More importantly, it shows our method learns to compromise label recovering but focus on improving segmentation when too limited pixels are available at small downsampled size, while when downsampled size increase, the model quickly pick up label recover accuracy while maintaining segmentation performance, evidenced by the cost-performance analysis in Fig. 7 (b).

While the "optimal edge" approach performed well on histology dataset, object edges does not guarantee most informative location, and it will fail as in Cityscapes dataset [9] and DeepGlobe dataset [10]. For example, see the red arrows pointed locations in Fig. 8, edges of the windows misguided the edge-based sampler and resulted under sampling of surrounding textures, which eventually caused wall been miss-predicted as sky. The edge-based approach would also fail when each class of annotated region contain a complex mixture of unannotated sub-regions. For example, in Fig. 9, the annotated forest regions in the green boxed region contain many sub-regions of like gardens and bushes and the model with our method learnt to sample sparser within this region for better segmentation prediction.

5 Conclusion

In this work, we present a new method for learning to downsample ultra high-resolution images with spatially adaptive sampling density reflecting semantic importance at each location. We shown our method been able to combine advantages of prior edge-based sampling method, but further improve by optimising sampling at locations that "uniform" and "optimal approaches" may fail. Our method is light weighted and can be flexibility combined with existing segmentation method without modifying architecture. It would enable a better cost-performance trad-off on segmentation with limited budget.

Acknowledgements.

We acknowledge the EPSRC grants EP/R006032/1, EP/M020533/1, the CRUK/EPSRC grant NS/A000069/1, and the NIHR UCLH Biomedical Research Centre which supported this research

References

- [1] Xueyang Wang, Xiya Zhang, Yinheng Zhu, Yuchen Guo, Xiaoyun Yuan, Liuyu Xiang, Zerun Wang, Guiguang Ding, David Brady, Qionghai Dai, et al. Panda: A gigapixel-level human-centric video dataset. In *Proceedings of the IEEE/CVF Conference on Computer Vision and Pattern Recognition*, pages 3268–3278, 2020.
- [2] Emmanuel Maggiori, Yuliya Tarabalka, Guillaume Charpiat, and Pierre Alliez. Can semantic labeling methods generalize to any city? the inria aerial image labeling benchmark. In *2017 IEEE International Geoscience and Remote Sensing Symposium (IGARSS)*, pages 3226–3229. IEEE, 2017.
- [3] Chetan L Srinidhi, Ozan Ciga, and Anne L Martel. Deep neural network models for computational histopathology: A survey. *arXiv preprint arXiv:1912.12378*, 2019.
- [4] Wuyang Chen, Ziyu Jiang, Zhangyang Wang, Kexin Cui, and Xiaoning Qian. Collaborative global-local networks for memory-efficient segmentation of ultra-high resolution images. In *Proceedings of the IEEE Conference on Computer Vision and Pattern Recognition*, pages 8924–8933, 2019.
- [5] Dmitrii Marin, Zijian He, Peter Vajda, Priyam Chatterjee, Sam Tsai, Fei Yang, and Yuri Boykov. Efficient segmentation: Learning downsampling near semantic boundaries. In *Proceedings of the IEEE/CVF International Conference on Computer Vision*, pages 2131–2141, 2019.
- [6] Liang-Chieh Chen, Yi Yang, Jiang Wang, Wei Xu, and Alan L Yuille. Attention to scale: Scale-aware semantic image segmentation. In *Proceedings of the IEEE conference on computer vision and pattern recognition*, pages 3640–3649, 2016.
- [7] Ke Sun, Yang Zhao, Borui Jiang, Tianheng Cheng, Bin Xiao, Dong Liu, Yadong Mu, Xinggang Wang, Wenyu Liu, and Jingdong Wang. High-resolution representations for labeling pixels and regions. *arXiv preprint arXiv:1904.04514*, 2019.
- [8] Andrew Tao, Karan Sapra, and Bryan Catanzaro. Hierarchical multi-scale attention for semantic segmentation. *arXiv preprint arXiv:2005.10821*, 2020.
- [9] Marius Cordts, Mohamed Omran, Sebastian Ramos, Timo Rehfeld, Markus Enzweiler, Rodrigo Benenson, Uwe Franke, Stefan Roth, and Bernt Schiele. The cityscapes dataset for semantic urban scene understanding. In *Proceedings of the IEEE conference on computer vision and pattern recognition*, pages 3213–3223, 2016.
- [10] Ilke Demir, Krzysztof Koperski, David Lindenbaum, Guan Pang, Jing Huang, Saikat Basu, Forest Hughes, Devis Tuia, and Ramesh Raskar. Deepglobe 2018: A challenge to parse the earth through satellite images. In *The IEEE Conference on Computer Vision and Pattern Recognition (CVPR) Workshops*, June 2018.
- [11] Liang-Chieh Chen, George Papandreou, Iasonas Kokkinos, Kevin Murphy, and Alan L Yuille. Semantic image segmentation with deep convolutional nets and fully connected crfs. *arXiv preprint arXiv:1412.7062*, 2014.
- [12] Bharath Hariharan, Pablo Arbeláez, Ross Girshick, and Jitendra Malik. Hypercolumns for object segmentation and fine-grained localization. In *Proceedings of the IEEE conference on computer vision and pattern recognition*, pages 447–456, 2015.
- [13] Guosheng Lin, Anton Milan, Chunhua Shen, and Ian Reid. Refinenet: Multi-path refinement networks for high-resolution semantic segmentation. In *Proceedings of the IEEE conference on computer vision and pattern recognition*, pages 1925–1934, 2017.
- [14] Olaf Ronneberger, Philipp Fischer, and Thomas Brox. U-net: Convolutional networks for biomedical image segmentation. In *International Conference on Medical image computing and computer-assisted intervention*, pages 234–241. Springer, 2015.
- [15] Hengshuang Zhao, Jianping Shi, Xiaojuan Qi, Xiaogang Wang, and Jiaya Jia. Pyramid scene parsing network. In *Proceedings of the IEEE conference on computer vision and pattern recognition*, pages 2881–2890, 2017.
- [16] Tsung-Yi Lin, Piotr Dollár, Ross Girshick, Kaiming He, Bharath Hariharan, and Serge Belongie. Feature pyramid networks for object detection. In *Proceedings of the IEEE conference on computer vision and pattern recognition*, pages 2117–2125, 2017.
- [17] Jifeng Dai, Haozhi Qi, Yuwen Xiong, Yi Li, Guodong Zhang, Han Hu, and Yichen Wei. Deformable convolutional networks. In *Proceedings of the IEEE international conference on computer vision*, pages 764–773, 2017.

- [18] Max Jaderberg, Karen Simonyan, Andrew Zisserman, and Koray Kavukcuoglu. Spatial transformer networks. *arXiv preprint arXiv:1506.02025*, 2015.
- [19] Adria Recasens, Petr Kellnhofer, Simon Stent, Wojciech Matusik, and Antonio Torralba. Learning to zoom: a saliency-based sampling layer for neural networks. In *Proceedings of the European Conference on Computer Vision (ECCV)*, pages 51–66, 2018.
- [20] Angelos Katharopoulos and François Fleuret. Processing megapixel images with deep attention-sampling models. *arXiv preprint arXiv:1905.03711*, 2019.
- [21] Yiqiu Shen, Nan Wu, Jason Phang, Jungkyu Park, Gene Kim, Linda Moy, Kyunghyun Cho, and Krzysztof J Geras. Globally-aware multiple instance classifier for breast cancer screening. In *International Workshop on Machine Learning in Medical Imaging*, pages 18–26. Springer, 2019.
- [22] Ross Girshick, Jeff Donahue, Trevor Darrell, and Jitendra Malik. Rich feature hierarchies for accurate object detection and semantic segmentation. In *Proceedings of the IEEE conference on computer vision and pattern recognition*, pages 580–587, 2014.
- [23] Fangting Xia, Peng Wang, Liang-Chieh Chen, and Alan L Yuille. Zoom better to see clearer: Human and object parsing with hierarchical auto-zoom net. In *European Conference on Computer Vision*, pages 648–663. Springer, 2016.
- [24] Ross Girshick. Fast r-cnn. In *Proceedings of the IEEE international conference on computer vision*, pages 1440–1448, 2015.
- [25] Kaiming He, Georgia Gkioxari, Piotr Dollár, and Ross Girshick. Mask r-cnn. In *Proceedings of the IEEE international conference on computer vision*, pages 2961–2969, 2017.
- [26] Chen Jin, Ryutaro Tanno, Moucheng Xu, Thomy Mertzaniidou, and Daniel C Alexander. Foveation for segmentation of mega-pixel histology images. In *International Conference on Medical Image Computing and Computer-Assisted Intervention*, pages 561–571. Springer, 2020.
- [27] Nanyang Wang, Yinda Zhang, Zhuwen Li, Yanwei Fu, Wei Liu, and Yu-Gang Jiang. Pixel2mesh: Generating 3d mesh models from single rgb images. In *Proceedings of the European Conference on Computer Vision (ECCV)*, pages 52–67, 2018.
- [28] Georgia Gkioxari, Jitendra Malik, and Justin Johnson. Mesh r-cnn. In *Proceedings of the IEEE International Conference on Computer Vision*, pages 9785–9795, 2019.
- [29] Lars Mescheder, Michael Oechsle, Michael Niemeyer, Sebastian Nowozin, and Andreas Geiger. Occupancy networks: Learning 3d reconstruction in function space. In *Proceedings of the IEEE Conference on Computer Vision and Pattern Recognition*, pages 4460–4470, 2019.
- [30] Maxim Tatarchenko, Alexey Dosovitskiy, and Thomas Brox. Octree generating networks: Efficient convolutional architectures for high-resolution 3d outputs. In *Proceedings of the IEEE International Conference on Computer Vision*, pages 2088–2096, 2017.
- [31] Scipy is open-source software for mathematics, science, and engineering. <https://docs.scipy.org/doc/scipy/reference/generated/scipy.interpolate.griddata.html>. Accessed: 2021-03-23.
- [32] Kaiming He, Xiangyu Zhang, Shaoqing Ren, and Jian Sun. Delving deep into rectifiers: Surpassing human-level performance on imagenet classification. In *Proceedings of the IEEE international conference on computer vision*, pages 1026–1034, 2015.
- [33] Diederik P Kingma and Jimmy Ba. Adam: A method for stochastic optimization. *arXiv preprint arXiv:1412.6980*, 2014.

Supplementary Material: Learning to Downsample for Segmentation of Ultra-High Resolution Images

A Appendix

Here we provide additional results and various ablation studies and implementation details that not been presented in the main paper. We also attach our code in the separate zip file submitted together in supplementary materials.

Contents

A.1 Apple-to-apple comparison to the original "optimal edge" [5]	12
A.2 Learning to downsample at extreme downsampling rate on histology images	12
A.3 Investigate the learnt class distribution	13
A.4 Single segmentation loss: regularisation term is needed	14
A.5 Stage training: how much contribution from the <i>deformation module</i> and the <i>edge loss</i> ?	15
A.6 Motivational study: when would optimal edge fail?	16
A.7 Simulated "optimal edge" results	17
A.8 Datasets	17
A.9 Network Architectures and Implementation Details	19

A.1 Apple-to-apple comparison to the original "optimal edge" [5]

We use simulated "optimal edge" results in the main paper because our primary interests is investigate the benefits of learning to downsampling and simulate "optimal edge" within our framework is beneficial to design strict elementary controlled experiments. While here to enable more fair comparison to the original "optimal edge" [5] work, we perform experiments on Cityscapes dataset[9] at comparable pre-processing (central largest square crop) and training conditions (with PSP-net[15] and 1000 epoches). The results in Table 2 shown our method can outperform "optimal edge" [5] method on cityscapes dataset upto 3%.

Table 2: Comparing our method with original "optimal edge" published results [5] on Cityscapes dataset[9] in mIoU. Our results here are learnt at comparable pre-processing (central largest square crop) and training conditions (with PSP-net[15] and 1000 epoches).

downsampled size	uniform	optimal edge[5]	ours
64	0.29	0.32	0.35
128	0.40	0.43	0.45
256	0.54	0.54	0.55

A.2 Learning to downsample at extreme downsampling rate on histology images

To further verify how our method perform at extream downsampling on histology images, in Fig. 11 and Fig. 12, we show two visual examples when downsampling rate of 50 times at each dimension applied to PCa-Histo dataset, and the corresponding quantitative results are given in the trade-off plot in Fig. 10 (the first downsample rate at 0.0004). Consistent to quantitative results, **our method can still perform well comparing to ground truth and significantly better than "uniform" baseline at such extreme downsampling rate, which leads to better cost-performance trade-off.** The read line in Fig. 10 indicated to achieve same final prediction accuracy, **the "uniform" baseline require to calculate 325% more pixels comparing to our method.** Our method perform especially well

for the most clinically important classes, **Gleason Grade 3 and Gleason Grade 4**. The sampling locations shown as masked blue dots in Fig. 11 and Fig. 12 also indicated our method learnt to sample densely at clinical important and challenge regions (e.g. cancerous nuclei and tissues) while sample sparsely at less informative regions (e.g. background), which lead to consistent improvement over uniform sampling on segmentation accuracy.

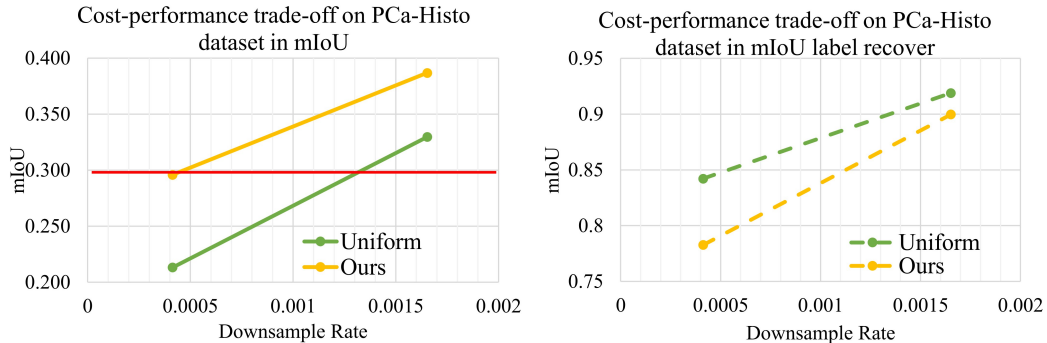


Figure 10: Cost-performance trade-offs on PCa-Histo dataset at extreme downsample rate at 0.0004. Our method perform significantly better than "uniform" baseline and leads to better cost-performance trade-off. The "uniform" baseline require to calculate 325% more pixels comparing to our method at the red line. Downsample rate is calculated by divide the total number of pixels after downsampling by original, which determines the size of the input and reflects the amount of computation required.

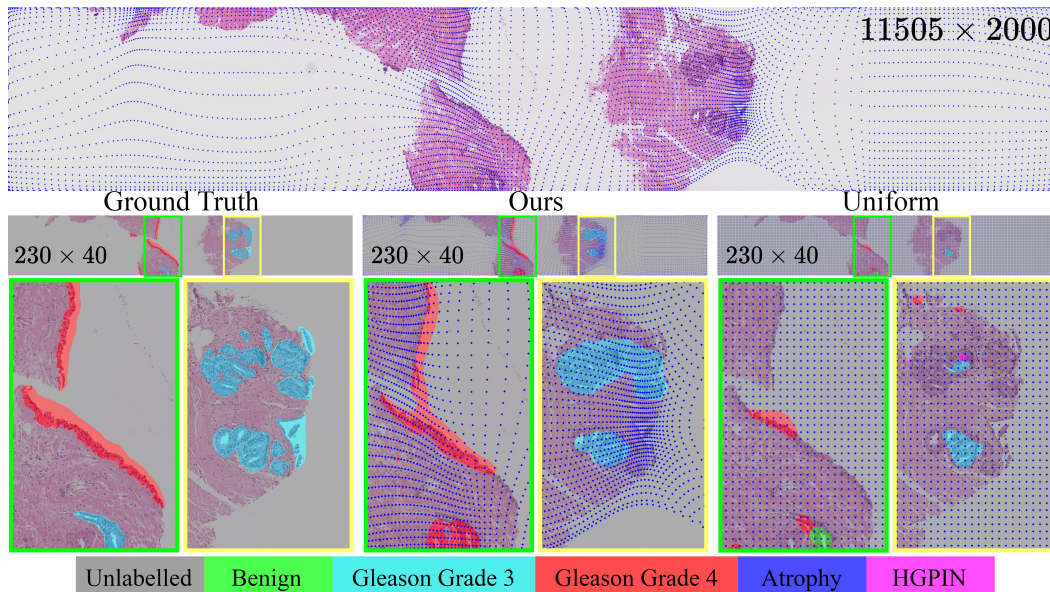


Figure 11: Qualitative example on PCa-Histo dataset (2) where segmentation performed on 50 times (at each dimension) downsampled image. Predictions are masked over and sampling locations are shown in blue dots.

A.3 Investigate the learnt class distribution

To verify our *deformation module* learnt to downsample denser at important regions/classes effectively, we monitor class frequency change after downsample the label of validation images with our learnt downsampler, as shown in Fig. 13. To have a direct evaluation of whether a class has been sampled denser or sparser comparing to its original frequency, we calculate the sampling frequency ratio with respect to original pixel frequency.

The results indicated the *deformation module* learnt to adjust sampling strategy so that more pixels are "invested" to important regions/classes and less from less informative region/classes, and lead to optimal overall segmentation accuracy. For example, the *deformation module* learnt to

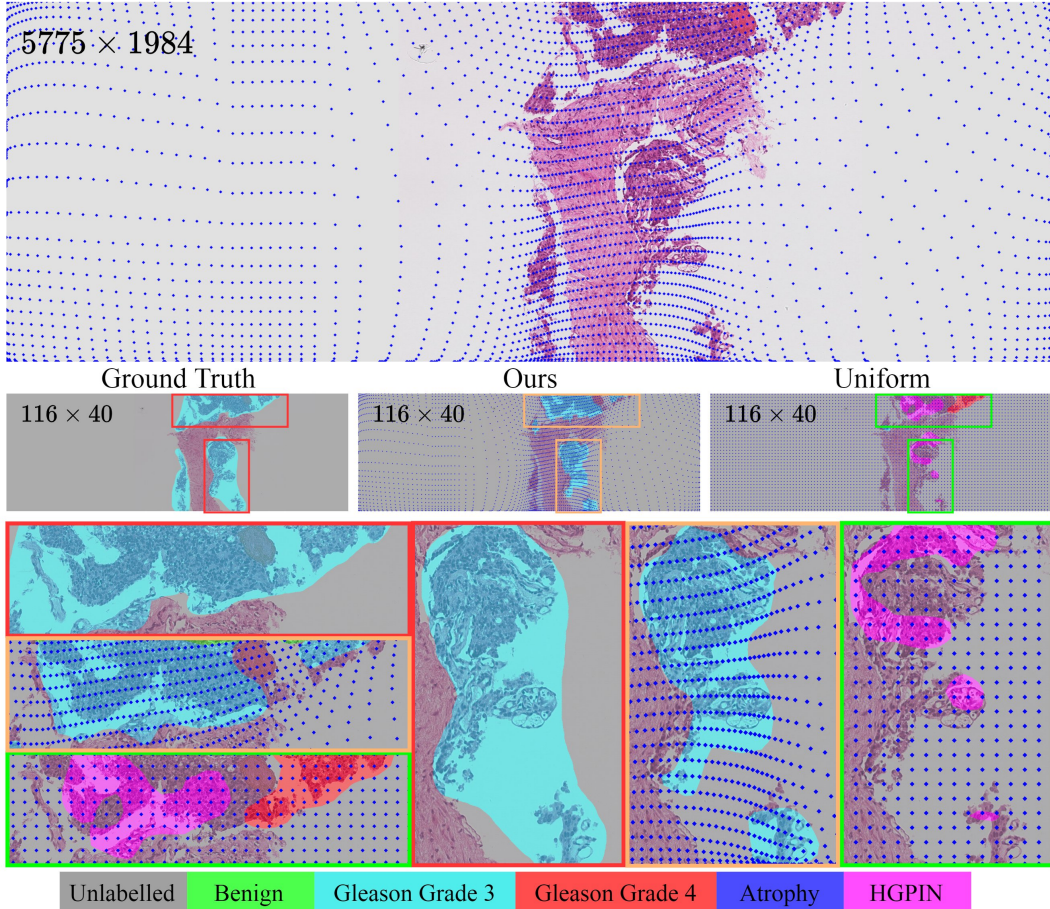


Figure 12: Qualitative example on PCA-Histo dataset (1) where segmentation performed on 50 times (at each dimension) downscaled image. Predictions are masked over and sampling locations are shown in blue dots.

sample less (shown as negative sampling frequency ratio) in the "Background" class in the PCA-Histo dataset (Fig. 13 (a)) and "road" and "sky" classes in the cityscapes[9] dataset (Fig. 13 (b)), in both cases those classes can be considered as potential "background" with common knowledge. However, **our method also shown ability to adjust sampling strategy on more complex dataset where "background class" is less obvious.** For example, in DeepGlobe[10] dataset, only the "Urban" class has been learnt to sample densely (with positive sampling frequency ratio) while all other classes has been learnt to sample slightly sparsely (Fig. 13 (c)), although considered as important "foreground class" with common knowledge. Such slight contradict to common knowledge sampling strategy however leads to boosted segmentation accuracy (see Fig. 17 and Fig. 7 in the main paper). The learnt distribution on the DeepGlobe dataset also **verified our argument that the manual designed *sample denser around object edge strategy as the "optimal edge" [5] method may fail when object boundary is less informative,*** which is justified in the main results as "optimal edge" based line performed significantly poorer than the "uniform" baseline Fig. 17.

A.4 Single segmentation loss: regularisation term is needed

In this section we show evidence to justify our claim in the main text: **straight transfer prior learning to downsample for classification work [19] to segmentation task and optimising the joint system at pixel level with single *segmentation loss* is not trivial.** We present the result when our framework trained with single *segmentation loss*, referred to as "ours - single loss", and compare with our method trained with the joint loss of *segmentation loss* and *edge loss* (as regularisation term), referred to as "ours - joint loss", as well as baselines in Fig. 14. First, the results indicates **the *edge loss* regularisation term is needed on top of the *segmentation loss* and can consistently leads to best results across**

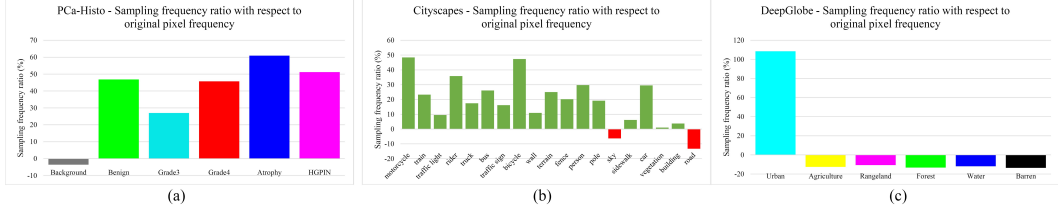


Figure 13: Sampling frequency ratio with respect to original pixel frequency. The higher the value the denser the learnt sampling comparing to uniform. Our method shows able to learn to adjust sampling either when foreground and background classes are clear (PCA-Histo and Cityscapes[9]) and when less clear (DeepGlobe[10]). Results are from three datasets: (a) a local prostate cancer histology dataset (PCA-Histo) at dynamic downsampled size of 80×800 pixels (b) Cityscapes[9] at downsampled size of 64×128 pixels and (c) DeepGlobe[10] at downsampled size of 300×300 pixels.

all datasets, although single *segmentation loss* could work by outperforming the "uniform" baseline on DeepGlobe and PCA-Histo dataset, but could also fail on Cityscapes dataset. Secondly, **the contribution of the edge loss regularisation term vary over datasets**. Specifically, in PCA-Histo dataset the edge is effectively guiding a better sampling strategy given the significant performance boost from "uniform" to "optimal edge" and from "ours - single loss" to "ours - joint loss"; however in DeepGlobe dataset the edge alone is not helping given the "optimal edge" significantly under-performed "uniform", while "ours - joint loss" can be further improved from "ours - single loss" by adding the *edge loss*, which already outperformed "uniform"; lastly in Cityscapes dataset is shown only when the *segmentation loss* combined with the *edge loss* can boost performance, because both "optimal edge" and "ours - single loss" both under-performed than "uniform". We further investigate the compound contribution from the *segmentation loss* and the *edge loss* on the Cityscapes[9] dataset in the next section.

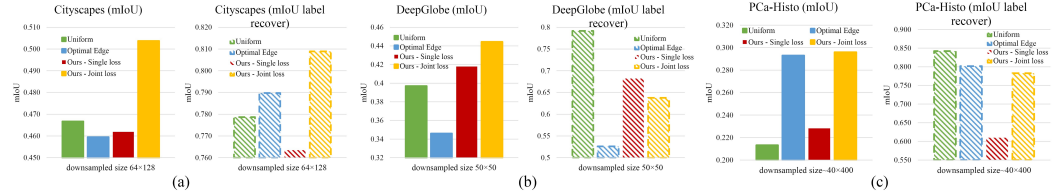


Figure 14: Comparison of our learn-to-downsample strategy with single loss (segmentation loss) versus joint loss (segmentation loss and edge loss). A key observation here is straight transfer prior learning to downsample for classification work [19] to segmentation task would not work and adding the edge loss regularisation term is necessary. Results for "uniform" and "optimal edge" baselines are included as references. Results are from three datasets: (a) Cityscapes[9] (b) DeepGlobe[10] and (c) a local prostate cancer histology dataset (PCA-Histo).

A.5 Stage training: how much contribution from the deformation module and the edge loss?

To better understand the compounded contribution from the *segmentation loss* and the *edge loss* on the Cityscapes[9] dataset, we break the whole training into two stages, and at each stage we optionally switch on/off the two loss terms to separate and investigate their contribution. First, we separately train each module with single loss, referred to as "stage - single loss" in Fig. 15. Specifically, we singularly train the downsampler, the *deformation module*, while freeze the the *segmentation module* in the first stage with single *edge loss*, and in the second stage we freeze the *deformation module* and only train the *segmentation module* with single *segmentation loss*. The "stage - single loss" strategy is a two stage training strategy that most similar to the original "optimal edge" [5] and its results represents the contribution of "edge loss" term. On top of "stage - single loss", we modify the second stage by jointly train both module with both the *segmentation loss* and the *edge loss*, referred to as "stage - joint loss". The "stage - joint loss" result represents contribution from our method. The results in Fig. 15 shows that **contribution from singularly "edge loss" term is limited**, where "stage - single loss" under-performed than "uniform" by 6% in mIoU. While **contribution from our joint trained system is significant**, where "stage - joint loss" performed close to "uniform" and slightly better than "ours - single loss" and "optimal edge". The improvement from "stage - joint loss" over "ours - single loss" also indicated the contribution from the *edge loss*.

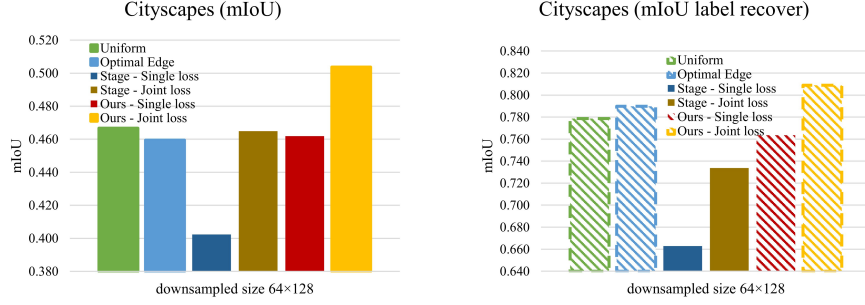


Figure 15: Comparison between two-stage training vs joint training of our approach on Cityscapes. A key insight is contribution from singularly "edge loss" term is limited while contribution from our joint trained system is significant. Results for "uniform" and "optimal edge" baselines are included as references. Results are from Cityscapes[9] datasets at downsampled size of 64×128 .

A.6 Motivational study: when would optimal edge fail?

The optimal edge sampler (SoTA): The "optimal edge" sampler proposed by [5], **assume that for better segmentation quality more pixels should be sampled near semantic boundaries**. Based on this hypothesize, they proposed to separately train a non-uniform down-sampling network minimizing two competing energy terms "sampling close to semantic boundaries" and "sampling close to uniform sampling locations". **A temperature term λ is used to balance between the two energies, whose value is empirically recommend to 1 by [5]**. Formally, let $\mathbf{b}[i, j]$ be the spatial coordinates of a pixel on the semantic boundary that is the closest to a sampling coordinate $(\mathbf{u}[i, j], \mathbf{v}[i, j])$. They train an "optimal edge" sampler \mathbf{G}_e minimising the energy:

$$\mathbf{E}(\mathbf{G}_e(i, j)) = \sum_{i, j} \|\mathbf{G}_e(i, j) - \mathbf{b}[i, j]\| + \lambda \sum_{i, j} \|\mathbf{G}_e(i, j) - \mathbf{G}_e(i', j')\|^2 \quad (3)$$

The first term in (3) minimise average distance to semantic boundaries, while the second term ² minimise average distance between neighboured sampling locations thus ensures the spatial structure after sampling is not distorted excessively.

When would optimal edge fail? In this section we perform an empirical analysis to investigate a key question: For the SoTA "optimal edge" [5] method, **would the empirically tuned one-size-fit-all configuration of the temperature term λ in Equation 3 give best performance?** The authors of [5] has shown learning an "optimal edge" sampler with different values of λ affects sampling density around label edges. Here we direct simulate such sampling behaviour by expanding sampling locations away from label edge at different distance in a Gaussian manner. In specific, we calculate edge from label then apply gaussian blur to generate a simulated deformation map to guide sampling in our framework. **We note that this simulated sampler can be considered as an "theoretical upper-bound" of the predicted "optimal edge" sampler because at inference time label won't be accessible.**

To simplify the problem and better design element controlled experiments on Cityscapes dataset, **we simplify the original 19-classes segmentation task into 19 binary segmentation tasks**. For each binary segmentation task, we consider one selected target class as foreground and all other classes as background. We generate a set samplers $\{\mathbf{G}_u, \mathbf{G}_{e_1}, \dots, \mathbf{G}_{e_n}\}$ and reverse samplers $\{\mathbf{G}_u^{-1}, \mathbf{G}_{e_1}^{-1}, \dots, \mathbf{G}_{e_n}^{-1}\}$, representing one "uniform" and 5 "optimal edge" samplers/reverse samplers. Each of the 1-5 "optimal edge" sampler have increasing sampling density around edge. Each of the $n = 5$ "optimal edge" approach have sampling locations Gaussian expanding away from label edge at fixed distance (determined by Gaussian blur radius) ranging from 1 to 21 pixels, with an incremental step of 2 pixels. With each sampler/reverse sampler, we first calculate **IoU** label recovery directly from label \mathbf{Y} , to investigate impact of sampling density around edge on the pure downsampling and upsampling related error. We then train a set segmentation networks with each sampler/reverse sampler and calculate the **IoU**, to investigate impact of sampling density around edge on the compound error.

²Here i', j' are the neighbouring pixels with a distance of 1 pixel to i, j (i.e. four in 2D), that meeting constrains $|i - i'| + |j - j'| = 1$.

Fig. 16 (a) shows the best **IoU** label recovery result for each class (row) across all samplers/reverse samplers in different color. Fig. 16 (b) shows **IoU** for 6/19 classes (each as a group of bar plots) across all samplers/reverse samplers (each bar plot in a group). It is clear that there is no “one-size-fits-all” sampling density around edge for “optimal edge” approach leads to the best performance for neither **IoU** label recovery nor **IoU** over all experimented individual classes. Fig. 16 (c) illustrates visually the variation of predictions with various sampling density for the two classes. These observations altogether imply that **both the standard “uniform” and the SoTA “optimal edge” sampling scheme with a pre-set sampling density around edge are sub-optimal, highlighting the potential benefits of a more intelligent strategy that can adaptively configure the most informative non-uniform sampling configuration to describe the local patterns at a given location.**

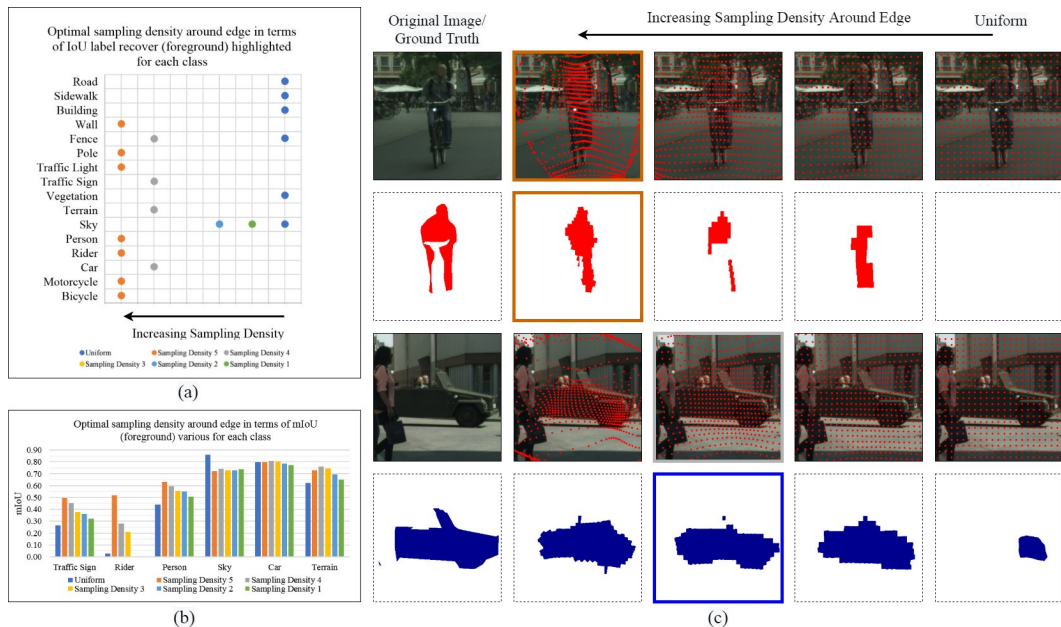


Figure 16: Quantitative (a-b) and qualitative evidence (c) that the optimal sampling density around edge varies over classes (a-b) and locations (c). (a): **IoU** (foreground) calculated, without training, with different sampling density around edge, where best performance for each class is highlighted (see Legends for references). (b): **IoU** (foreground) for each class over different sampling density around edge (see Legends for references). (c) Visual comparison of ground truth/ predictions (in second and fourth rows) with various sampling density for the two classes, shown in red and blue color. Sampling locations are masked on original image in red dots in the first and third rows. All experiments performed on Binary Segmentation on Cityscapes with downsampled size of 64×128 from 1024×2048 pixels. We evaluate on 1/10th subset of the full Cityscapes validation dataset, where 3 out of the 19 classes are under-represented and thus not shown here.

A.7 Simulated "optimal edge" results

As declared in the main text, our "optimal edge" baseline is the best performed segmentation network trained from a set directly simulated "optimal edge" downsamplers, each with a fixed sampling density around edges. Here we present full segmentation accuracy with the set directly simulated "optimal edge" downsamplers, for each of the three datasets.

A.8 Datasets

In this work, we verified our method on three segmentation datasets: DeepGlobe aerial scenes segmentation dataset [10], CityScape urban scenes segmentation dataset [9] and PCa-Histo medical histopathological segmentation dataset.

The **DeepGlobe** [10] dataset has 803 high-resolution (2448×2448 pixels) images of aerial scenes. There are 7 classes of dense annotations, 6 classes among them are used for training and evaluation

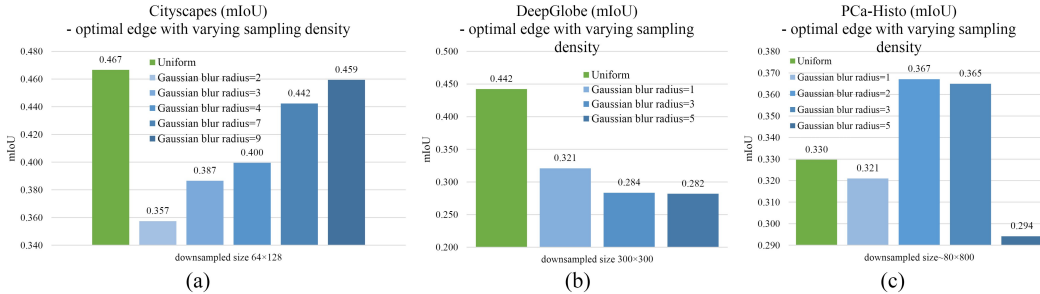


Figure 17: Simulated "optimal edge" results, with a set directly simulated "optimal edge" downsamplers, each with different fixed sampling density determined by gaussian blur radius. Best performed result is selected and referred to as the "optimal edge" result presented in the main paper. Results are from three datasets: (a) Cityscapes[9] (b) DeepGlobe[10] and (c) a local prostate cancer histology dataset (PCa-Histo).

according to [10]. We randomly split the dataset into train, validate and test with 455, 207, and 142 images respectively.

The **Cityscape** [9] dataset contains 5000 high-resolution (2048×1024 pixels) urban scenes images collected across 27 European Cities. The finely-annotated images contain 30 classes, and 19 classes among them are used for training and evaluation according to [9]. The 5000 images from the Cityscape are divided into 2975/500/1525 images for training, validation and testing.

The **PCa-Histo**: dataset contain 266 ultra-high resolution whole slide images, from 33 distinct biopsies. The size of the images ranged from 250800 pixels to 4088000 pixels. Each pixel is annotated into one out of six classes: Unlabelled, Benign, Gleason Grade 3, Gleason Grade 4, Atrophy, HGPIN (see Table 3 for explanations of each class). Among the six classes, informative classes are underrepresented comparing to Unlabelled class (see Table 3). We random split the dataset into 200 training, 27 validation and 39 test images. This dataset has varying size, with height (the short axis) range between 229 to 2000 pixels (1967.5 ± 215.5 pixels), width (the long axis) range between 3386 to 20440 pixels (9391.9 ± 4793.8 pixels) and Aspect Ratio (AP) range between 1.69 to 33.9 (5.04 ± 3.54). The downsample size of this dataset is calculated as follows: with a dynamic downsample size of for example 80×800 , for each image, we calculate two candidate downsample sizes by either downsample the short axis to 80 or the long axis to 800 while in either case we keep AP unchanged. Then we select the one downsample size that have less total pixels. For example, for an image with size 368×7986 pixels, we have candidate downsample sizes of 200×4340 pixels or 36×800 pixels, and we will use downsample size of 36×800 in our experiment. Also we apply batch size per gpu node of 1 because of the varying downsampled size of each image.

Table 3: Pixel frequency distribution of PCa-Histo dataset and explanation of each class

Label	Background	Benign	Gleason Grade 3	Gleason Grade 4	Atrophy	HGPIN
% pixels in dataset	93.99	0.97	1.23	3.35	0.26	0.20
Explanation	all unlabelled pixels	healthy	mild cancer	aggressive cancer	healthy noise	precursor legion

The prostate biopsies of PCa-Histo dataset are collected of 122 patients collected between 2010 and 2011. The identity of the patients is completely removed, and the dataset is used for research. The biopsies are a mixture of template and TRUS biopsies depending on where the tumour was located in the patient's prostate (UCLH uses multiparametric MRI to first locate the tumour before the biopsy). The biopsy cores were sliced, mounted on glass slides, and stained with H&E. From these, one slice of each of 220 cores were digitised using a Leica SCN400 slide scanner. The biopsies were digitised at 5, 10 and 20 magnification. At 20 magnification (which is the magnification used by histopathologists to perform Gleason grading), the pixel size is $0.55 \mu\text{m}^2$.

A.9 Network Architectures and Implementation Details

Architectures: The *deformation module* is defined as a small CNN architecture comprised of 4 convolution layers, each with 3×3 kernels followed by BatchNorm and Relu. The number of kernels in each respective layer is $\{24, 24, 3, 1\}$. A softmax layer is added at the end. All convolution layers are initialised following He initialization [32]. The *segmentation module* was defined as a deep CNN architecture, with HRNetV2-W48 [7] applied in all datasets, and PSP-net[15] as a sanity check in Cityscapes dataset. The segmentation network HRNetV2-W48 is pre-trained on Imagenet dataset as provided by the author [7]. In all settings, the size of deformation map d are either consistent or twice the size of downsampled image.

Training: For all experiments, we employ the same training scheme unless otherwise stated. We optimize parameters using Adam [33] with initial learning rate of $1e10^{-3}$ and $\beta = 0.9$, and train for 200 epochs on DeepGlobe, 250 epochs on PCa-Histo dataset, and 125 epochs on Cityscapes dataset. We use batch size of 4 for the Cityscapes dataset[9] and the DeepGlobe dataset[10] and batch size of 2 for PCa-Histo dataset. We employ step decay learning rate policy. We scale the *edge loss* 100 times so it is in the same scale with the *segmentation loss*. During training of the segmentation network we do not include upsampling stage but instead downsample the label map. For all datasets, we take whole image to downsample as input, without any crop. During training we augment data by random left-right flipping. We All networks are trained on 2 GPUs from internal cluster (machine models: gtx1080ti, titanxp, titanx, rtx2080ti, p100, v100, rtx6000), with syncBN.